Quantum contributions to Coulomb-explosion imaging revealed by trajectory-surface-hopping molecular dynamics

Vaibhav Singh,[1] Chuan Cheng,[2] Thomas Weinacht,[2] and Spiridoula Matsika[1]
[1]*Department of Chemistry, Temple University, Philadelphia, Pennsylvania 19121, USA*
[2]*Department of Physics, Stony Brook University, Stony Brook, New York 11790, USA*

(Received 4 January 2024; accepted 23 April 2024; published 10 May 2024)

We compare trajectory-surface-hopping (TSH) calculations of the dissociation of quadruply charged formaldehyde molecules with basic classical calculations assuming Coulomb repulsion between singly charged atoms. The TSH calculations show very different dissociation dynamics from the classical Coulomb calculations, illustrating that Coulomb repulsion between point charges does not accurately describe the dissociation dynamics. By comparing the calculations with covariance measurements, we see much better agreement between the experiments and the TSH calculations, and evidence for the production of multiple electronic states of the tetracation via strong-field ionization.

DOI: 10.1103/PhysRevA.109.052813

I. INTRODUCTION

Coulomb-explosion imaging (CEI) has become a prominent technique to capture the instantaneous geometry of a molecule undergoing rapid structural changes. Hence, it has helped in the study of the ultrafast dynamics of several molecules [1–6]. In this approach, multiple ionization in the electric field of an intense ultrafast laser pulse can build up positive charge in a molecule, which causes the charged fragment ions to fly away due to Coulomb repulsion. Measuring the momenta of the fragments can then be used to recover the initial molecular geometry. This technique has helped provide structural and dynamical insight into an array of systems and processes, including the characterization of isomers [5–8], hydrogen migration [9–12], roaming [13], and visualization of conical intersections [14]. The most common approximation used to model the phenomenon is to assume that every atom or fragment acquires a charge of +1 and Coulombic forces are the only forces acting between the fragments or atoms, resulting in Coulomb explosion [2,3,9,15,16]. Besides this simplistic approach, there are a few studies where *ab initio* dynamics, which include quantum effects such as bonding and nonadiabatic couplings, have been used [12,13,17,18]. However, the theoretical modeling in these studies used a reduced dimensionality model, only included the ground state of the charged species, or examined only partial fragmentation. The work of Endo *et al.* [13], which is closer to the present study, compared calculations for the dissociation of D_2CO^{3+} using classical Coulombic forces and the *ab initio* potential energy surfaces of D_2CO^{3+} in the ground state. While their work found reasonable agreement between the two approaches, two of the three particles involved are point charges, and it is not clear whether such agreement generally extends to more complicated fragmentation involving multielectron fragment ions.

In this work we try to understand the four-body breakup of the deuterated formaldehyde tetracation (CD_2O^{4+}) due to Coulomb explosion using multireference electronic structure methods and on-the-fly nonadiabatic dynamics through semiclassical trajectory surface hopping (TSH) [19,20] on multiple surfaces. To check if an elementary approach of a charge per atom could be simulated with the Coulombic forces (CFs), we compare the CF results with the nonadiabatic dynamics. We find significant differences between the two calculations, including the formation of metastable CO^{2+} in the TSH dynamics. Thus, we show that the approximation of one charge per fragment or atom and pure classical Coulomb forces is insufficient to accurately treat dissociation. Experimental work by Cheng *et al.* [21] showed some evidence of metastable CO^{2+}, which can be explained by the results described here. This work is also unique in terms of the direct comparison of CF and TSH results with the experimental results that sets another example of why quantum principles can be important in describing processes involved during CEI.

II. METHODOLOGY

A. Electronic structure methods

The geometry of neutral formaldehyde was optimized at the density-functional theory [22,23] level of theory using the B3LYP [24–27] functional and 6-311+G(d) [28,29] basis set. The potential energy surfaces (PESs) of CH_2O^{4+} (which are identical to CD_2O^{4+}) were scanned along the C-O stretch and the symmetric C-H stretch at the 20-state-averaged–complete-active-space self-consistent field [20SA-CASSCF(8,8)] [30]/cc-pVDZ [31] level of theory using C_{2v} symmetry. Here five singlets and five triplets were calculated separately for each of the four irreducible representations of C_{2v} symmetry, i.e., A_1, B_1, B_2, and A_2, summing up to 20 singlets and 20 triplets. A large number of states were included in order to identify the lowest-energy states of the correct symmetry. Once that was done, the following discussion and dynamics focused on the first six singlet and four triplet states. The PESs of CO^{2+} singlets and triplets were also calculated at the 20SA-CASSCF(8,8)/cc-pvDZ level of theory, averaging over five singlet and five triplet states for each irreducible representation in C_{2v} symmetry (which again

 ©2024 American Physical Society

is 20 singlets and 20 triplets in total). Here the C_{2v} is used as a lower symmetry group to calculate the states of CO^{2+}, which has an actual symmetry of $C_{\infty v}$. The two-dimensional (2D) PESs of CH_2O^{4+} were also calculated as a function of C-O stretch and symmetric C-H stretches using the same 20SA-CASSCF(8,8)/cc-pVDZ level of theory. This active space was chosen after careful benchmarking of the vertical excitation energies with different active spaces, which is presented in Appendix A. The optimization was carried out using GAUSSIAN [32]. All of the CASSCF calculations were performed using the COLUMBUS software [33–35].

B. Dynamics

We carried out the dynamics starting from each one of the energetically lowest states of CD_2O^{4+}, i.e., the first six singlet states and the first four triplet states, for a total of ten independent dynamical runs. Deuterated formaldehyde was chosen for the dynamics because experiments were carried out on the same molecule. The molecular dynamics of the CD_2O^{4+} were calculated in two ways: first, by using only the classical equations of motion for four singly charged atomic ions, and second, using the semiclassical TSH approach [19,20]. For the first approach, because of the highly repulsive nature of the tetracation's PESs, it was assumed that the Coulomb explosion of CD_2O^{4+} would lead to the formation of C^+, O^+, D^+, and D^+. Hence, the simulation was performed by treating each charged atom (of +1) as a point charge with a mass equivalent to its atomic mass and a CF acting on it due to the other point charges. Alternatively, different partial charges can be used for the Coulombic forces, taking into account that when the tetracation is in equilibrium the charges are not equally distributed in the four atoms. This approach, however, becomes more unrealistic at far distances where all atoms are separated and they should have a charge of +1. Nevertheless, we compared trajectories using the two different choices of charges and the results did not change qualitatively. The partial charges on each atom of D_2CO^{4+} were calculated at the CASSCF level of theory. A time step of 0.0082 fs was used and the simulation was run for 50 fs. Two hundred initial conditions (ICs) containing the geometries and the initial velocities of CD_2O^{4+} were generated using the harmonic-oscillator Wigner distribution of the ground-state minimum of CD_2O. The frequencies were calculated at the B3LYP/6-311+G(d) level of theory. The same ICs were used for the dynamics performed with CF as well as TSH. The Wigner distribution code, as implemented in NEWTON-X, was used [36,37]. The codes for the dynamics with CF were implemented with PYTHON2.

For the TSH dynamics, the nuclear evolution of the ICs was treated classically using the velocity Verlet algorithm with a time step of 0.5 fs. The electronic energies, the nonadiabatic couplings, and the gradients along which these trajectories evolve were calculated at each time step, on the fly at the eight-state-averaged SA8-CASSCF(8,8)/cc-pvDZ and six-state-averaged SA6-CASSCF(8,8)/cc-pvDZ levels of theories for the dynamics on the singlet and triplet surfaces, respectively. The dynamics were set up to run for a total of 100 fs on S_0 and S_1, although almost all of them were completed by 50 fs. The generation of ICs and the TSH dynamics were done with the help of NEWTON-X [36,37]. A trajectory was eliminated if the total energy at any time step deviated by more than 0.5 eV from the energy at the previous time step or at time zero. The fewest switches surface hopping algorithm implemented in NEWTON-X was used to calculate hopping probability between nonadiabatic surfaces [38]. After a trajectory hops due to nonadiabatic coupling, its momentum is rescaled along the derivative coupling vector to conserve the total energy. Also, in the case of frustrated hopping, i.e., when a trajectory does not have enough energy to hop, the direction of its momentum is left unaltered. To deal with decoherence, the decoherence correction method of Grannuci and Persico [39] was used with a correction factor of 0.1 hartree [40]. The results of the TSH dynamics are shown for the first 50 fs, even though they were run for 100 fs. This is because most of the interesting phenomena occurred in the first 50 fs of the dynamics. Also, the trajectories on many states did not survive after 50 fs due to failure in the CASSCF calculation convergence or energy conservation failure (see Fig. 9 in Appendix D, where the C-O bond length vs time is plotted for 100 fs).

C. Experiment

The experiment makes use of a velocity map imaging (VMI) apparatus [41] outfitted with a Tpx3Cam camera [42]. The laser pulses originate from a commercial amplified Ti:sapphire laser system, which produces 30-fs laser pulses with 1 mJ of energy at a repetition rate of 1 kHz. The pulses are spectrally broadened in a stretched hollow core fiber (SHCF) [43–46] and compressed using chirped mirrors to a minimum duration of about 6 fs. The pulses (30 fs from the amplifier or 6 fs from the SHCF) are focused into our VMI apparatus to ionize molecules.

The sample, deuterated formaldehyde, is obtained by sublimation of paraformaldehyde-D_2 (purity 98%, Sigma-Aldrich) at 50 °C–60 °C. A skimmed molecular beam of sample molecules intersects the laser in the VMI apparatus.

The ionized fragments are accelerated toward the microchannel plates and phosphor screen under velocity-mapping conditions. The fluorescence from hits on the phosphor screen is imaged onto the camera with an $f/0.95$ lens. The 1-ns precision of the Tpx3Cam is sufficient to resolve the ion momenta along the time-of-flight direction, which can be used to reconstruct the full 3D vector momenta of ions [42,47].

III. RESULTS AND DISCUSSION

A. Dynamics

We first present the results of the TSH dynamics, which was run on six singlet and four triplet states of CD_2O^{4+}. Table I summarizes the fragmentation patterns observed, showing the number of three-body ($CO^{2+}/D^+/D^+$) and four-body ($C^+/O^+/D^+/D^+$) dissociative products formed by running the TSH dynamics on each state. The electronic energies of states at vertical ionization are also shown relative to the lowest singlet state of the tetracation S_0 (note that the lowest-energy state is a triplet T_1). Out of ten surfaces (six singlets and four triplets) on which the TSH dynamics was run, all supported the formation of CO^{2+} to various degrees. The dynamics on electronic states S_0, S_1, T_1, and T_3 yielded

TABLE I. Number of trajectories leading to three-body ($CO^{2+}/D^+/D^+$) or four-body ($C^+/O^+/D^+/D^+$) dissociation on each electronic state. Also provided are the respective energies and symmetries of electronic states at the Franck-Condon region. The electronic structure calculations were performed at the CASSCF(8,8)/cc-pVDZ level of theory. A total of 200 trajectories were run on each state and several of them failed before it was clear what the dissociation products were. The number of failed trajectories is shown in the last column.

State	Symmetry	E (eV)	No. of three-body trajectories	No. of four-body trajectories	No. of failed trajectories
S_0	$1\,^1B_1$	0.00	120	9	71
S_1	$1\,^1A_1$	0.19	94	17	89
S_2	$2\,^1A_1$	0.43	71	50	79
S_3	$1\,^1A_2$	0.90	68	51	81
S_4	$3\,^1A_1$	2.24	76	62	62
S_5	$1\,^1B_2$	2.68	34	119	47
T_1	$1\,^3B_1$	−1.60	137	41	22
T_2	$1\,^3A_2$	−0.37	65	105	30
T_3	$1\,^3B_2$	0.24	118	57	25
T_4	$2\,^3B_1$	1.22	81	90	29

a high number of three-body products. On the other hand, S_5 and T_2 were rich in producing four-body products. In order to better understand the origin of this behavior, we focus more on the ground state, i.e., T_1 surface, since the dynamics on the other states can be explained analogously.

For the CF approach, there are no excited states, so only one set of trajectories was run. Furthermore, one has to decide what charge should be used on each atom. Two obvious choices exist. One is to use a +1 charge on each atom, since this is the correct dissociation limit, after Coulomb explosion when all the atoms are far away from each other. However, when the atoms are still close to each other and there are still some bonding interactions, the charges are not +1. In that case, partial charges can be obtained from the *ab initio* calculations. These charges will be more appropriate initially, but a fractional charge on an atom is unrealistic when atoms are far from each other. We compared the dynamics for a few representative trajectories using the two different sets of charges and the results are shown in Fig. 1. Clearly, in both scenarios, atoms fly away from each other, exhibiting similar physics. So we will continue our comparisons with a full set of trajectories using +1 charges, which better represent the dissociation limit.

We then compare the TSH results with the dynamics run with CF and point charges. Results for the ground state T_1 are shown here, while results for the other states are shown in Appendix D. The idea is to compare the dynamics run with a semiclassical method (TSH) with entirely classical dynamics and check the validity of this elementary approach. Figure 2 shows the evolution of C-O and two C-D bond lengths with respect to time for the dynamics run on the T_1 state of CD_2O^{4+} for both sets of dynamics. The comparison between the CF and TSH dynamics clearly shows that the dynamics of the dissociation of the two C-D bonds are similar between the two approaches, which means that the two D^+ ions dissociate fast and classically, but the C-O dissociation behaves very differently. C-O dissociation using CF is very fast. On the other hand, only 41 trajectories out of 200 on T_1 dissociate within 50 fs when using TSH. Even those that dissociate

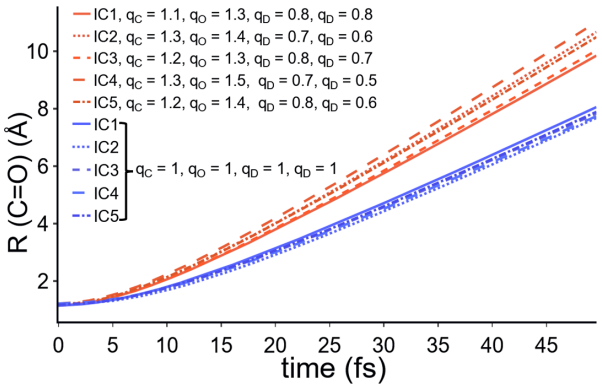

FIG. 1. CO bond length R(C=O) plotted for five trajectories IC1–IC5, starting from different initial conditions (ICs), simulated with CF in two ways: (i) $q = +1$ was assumed on each of the atoms C, O, D and D and (ii) the q, equal to Mulliken's partial charges on each of the atoms, were calculated at the MSCCF(8,8)/cc-pVDZ level of theory. The Mulliken charges for each trajectory are shown in the legend.

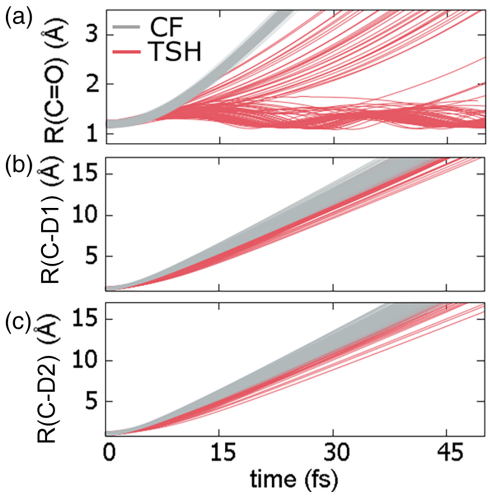

FIG. 2. Bond length of (a) C-O, (b) C-D1, and (c) C-D2 plotted vs time for the dynamics performed on the T_1 state of CD_2O^{4+} using simple classical Coulombic forces and trajectory surface hopping.

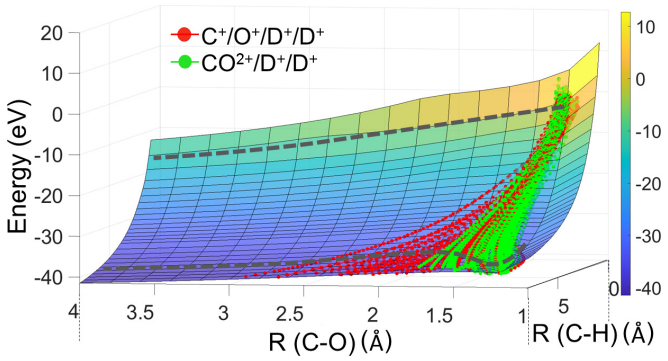

FIG. 3. 2D PES of the T_1 state along C-O and symmetric C-H bonds. Bifurcation of trajectories into the formation of the products $CO^{2+}/D^+/D^+$ (green) and $C^+/O^+/D^+/D^+$ (red) is shown. The 1D cuts of the PES along the gray dashed lines are shown in Fig. 4.

within 50 fs are much slower than in the classical case. This is because classical mechanics cannot capture the bonding nature of CO^{2+} once the two D atoms break away quickly. The internal coordinates vs time are also plotted for the TSH dynamics on other electronic states in Fig. 9 in Appendix D. All of the C-O plots show that the dissociation of CD_2O^{4+} can indeed form metastable CO^{2+} through all the electronic states of CD_2O^{4+}.

B. Potential energy surfaces

In order to understand the dynamics better, we examine the PESs of the electronic states of CD_2O^{4+} along the C-O and C-D (or C-H) bonds. Note that the PESs of the isotopes CD_2O^{4+} and CD_2O^{4+} are the same. Figure 3 shows the adiabatic T_1 two-dimensional surface of CD_2O^{4+} plotted against the C-O stretch and the symmetric C-D stretch. According to Fig. 2, the dissociation dynamics of the C-D bonds are symmetric, i.e., both are stretched at the same time, so it makes sense to plot PESs against the symmetric C-D stretch. The 200 TSH trajectories are also superimposed in Fig. 3. One can notice the bifurcation of trajectories in green and red. The 41 trajectories in red represent the trajectories where C-O dissociates to form the product $C^+/O^+/D^+/D^+$, whereas the trajectories shown in green form $CO^{2+}/D^+/D^+$. Some red trajectories overlap with the green trajectories, because they also dissociate but at longer C-D bond lengths, which are out of the range shown in this PES. The shape of the PES makes clear the reason for the formation of CO^{2+}. When the CD bonds are short (in intact CD_2O^{4+}), C-O is directly dissociative. However, as soon as the CD bonds start breaking, a minimum is formed along the CO bond, which can trap the population. Most of the trajectories (green lines in the figure) follow the gradient and get trapped in the well, although there are several trajectories that escape (red lines) and break the CO bond. In order to better understand the dynamics, we now consider cuts of the 2D PES along the C-O stretch for certain values of the C-D stretch.

Figure 4(a) shows CD_2O^{4+} PESs along the C-O stretch for six singlet and four triplet states. The configurations describing these states are shown in Appendix B. As expected, the PESs of all the states are dissociative because of their

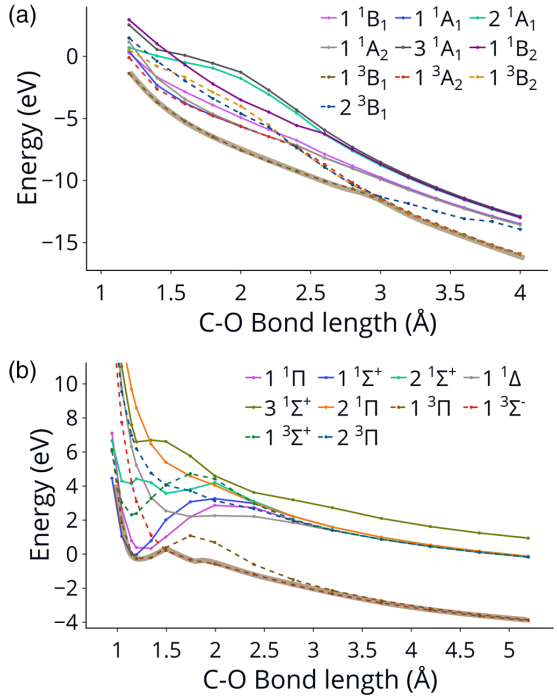

FIG. 4. PESs of six singlets (solid line) and four triplets (dashed line) calculated along the C-O stretch for (a) CH_2O^{4+} and (b) CO^{2+}. The calculations were carried out at the CASSCF(8,8)/cc-pVDZ level of theory. All of the energies in (a) are with respect to the energy of the lowest singlet state of CH_2O^{4+} at the neutral equilibrium geometry and in (b) are with respect to the energy of the CO^{2+} ground-state minimum. Here $1\,^3B_1$ and $1\,^3B_2$ of D_2CO^{4+} convert into the $1\,^3\Pi$ state of CO^{2+} for all the correlations between D_2CO^{4+} and CO^{2+} states (see Table II). The adiabatic T_1 state is highlighted with a thick transparent brown line.

Coulombic nature. The same is true for the PESs along the C-D stretch, as can be seen in Fig. 5. One can hypothesize (and it is confirmed by the dynamics) that since the mass of oxygen is 8 times (16 times) heavier than deuterium (hydrogen), the C-D(C-H) dissociation should be very fast compared

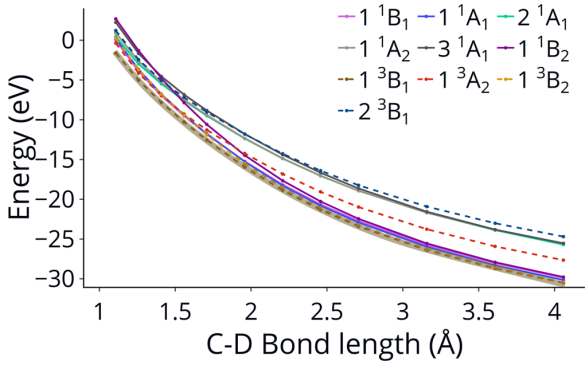

FIG. 5. PESs of six singlets (solid line) and four triplets (dashed line) calculated along the C-D (or C-H) stretch for CD_2O^{4+} (or CH_2O^{4+}). The calculations were carried out at the CASSCF(8,8)/cc-pVDZ level of theory. All of the energies are with respect to the S_0 state at the neutral equilibrium geometry of CH_2O^{4+}. The adiabatic T_1 state is highlighted with a thick transparent brown line.

TABLE II. Correspondence of D_2CO^{4+} states to CO^{2+} states. The corresponding vertical excitation energies (VEs) of CO^{2+} are also provided with respect to the S_0 minimum of CO^{2+}, which is $^1\Sigma^+$.

D_2CO^{4+} states	Corresponding CO^{2+} states	VEs (eV) of CO^{2+} states
$1\,^3B_1 + 1\,^3B_2$	$1\,^3\Pi$	0.08
$2\,^3B_1 + 2\,^3B_2$	$2\,^3\Pi$	6.97
$1\,^3A_2$	$1\,^3\Sigma^-$	4.21
$1\,^3A_1$	$1\,^3\Sigma^+$	2.31
$1\,^1B_1 + 1\,^1B_2$	$1\,^1\Pi$	0.79
$1\,^1A_1$	$1\,^1\Sigma^+$	0.00
$2\,^1A_1$	$2\,^1\Sigma^+$	4.14
$2\,^1A_2$	$1\,^1\Sigma^-$	9.81
$3\,^1A_1 + 1\,^1A_2$	$1\,^1\Delta$	6.31

to C-O dissociation in CD_2O^{4+} (CH_2O^{4+}). However, in that scenario, once the D atoms dissociate away from CD_2O^{4+}, the dissociation of C-O then should be controlled by the PESs of CO^{2+}. Figure 4(b) shows the PESs of CO^{2+}, calculated using SA20-CASSCF(8,8)/cc-pVDZ, which demonstrate that a few electronic states with high-energy barriers can support the formation of metastable CO^{2+}. Some of these states are $1\,^1\Sigma^+$, $1\,^1\Pi$, $1\,^3\Pi$, and $1\,^3\Sigma^+$ with energy barriers of 3.2, 2.5, 1.3, and 2.4 eV along the C-O stretch. Refer to Table II to correlate CH_2O^{4+} states to the CO^{2+} states and for excitation energies of CO^{2+}. The deep or shallow wells along the C-O stretch can hence support the formation of CO^{2+}. The depth of these wells defines the lifetimes of the metastable CO^{2+}, determining the tunneling rate through barriers.

In general, TSH dynamics cannot capture the tunneling of metastable populations through the energy barriers since it is a semiclassical method. However, the lifetimes of metastable CO^{2+} have been discussed previously in the literature. Both experimental [48–51] and theoretical results [52] have shown that the lifetimes of the first few vibronic states can range from a few picoseconds to seconds for states such as the $v = 0, 1$ vibrational states of $1\,^3\Pi$. Since the time of flight of the VMI apparatus used in the experiment is on the order of microseconds (which is more than the lifetimes of most of the states), the experiments can capture the signature of metastable CO^{2+}.

C. Comparison with experiment

We compare our CF and TSH calculations with the experiment using a native frame analysis in order to account for the sequential dissociation of CO^{2+}. The experimental signal has been presented in detail in Ref. [21] and here the relevant plot is used for comparisons with theory. Native frame analysis has been very helpful in distinguishing between the sequential and concerted dynamics using the Jacobi coordinates, especially in the case of three-body dissociation [7,53]. This analysis aims to compare an observable, here the kinetic energy of CO^{2+} with respect to the momenta of the two D^+ ions ($\mathcal{E}_{CO}$) calculated using theory and experiment in the native frame. Note that, due to complications in the measurements, CH_2O^{4+} was used rather than CD_2O^{4+} for the native frame analysis.

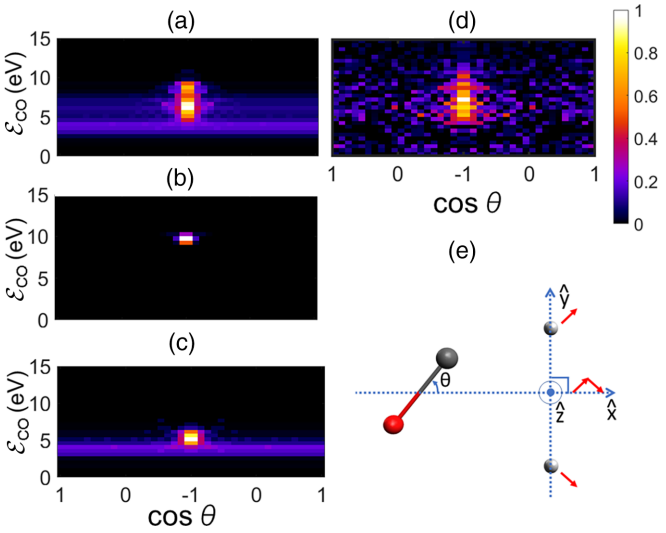

FIG. 6. Distributions of dissociation energies of CO^{2+} ($\mathcal{E}_{CO}$) against the cosine of the angle defined in the native frame θ for (a) TSH trajectories on all ten states, (b) CF, (c) TSH trajectories on T_1, T_2, and S_0, and (d) experimental results for a 6-fs laser pulse (taken from Ref. [21]). (e) Image explaining the axes used for the native frame analysis.

The relevant axes for the analysis can be seen in Fig. 6(e), where the x axis is along the sum of momenta vectors of both the D cations (red arrows), the y axis is along the difference between them, and the z axis is the cross vector of x and y axes. Also, θ is the angle of rotated CO^{2+} with respect to the x axis. In order to calculate $\mathcal{E}_{CO}$ when running TSH we need to switch to classical Coulombic forces after the trajectories fail because they almost never reach a point where the Coulomb interactions are negligible. At the point of switching, there is an abrupt change from a PES calculated using quantum chemistry (QPES) and CF (CPES), as seen in Fig. 8 in Appendix C. Hence, the $\mathcal{E}_{CO}$ values were shifted with the difference between the QPES and CPES at the last point of the TSH trajectory such that the abrupt change between QPES to CPES is compensated. This correction is described in detail in Appendix C.

In Fig. 6 we compare the experimental results obtained with a 6-fs laser to our TSH and CF calculations analyzed in the native frame. The figure shows the 2D distribution of calculated $\mathcal{E}_{CO}$ along the $\cos\theta$ values for TSH dynamics on all states [Fig. 6(a)], CF dynamics [Fig. 6(b)], TSH dynamics on T_1, T_2, and S_0 [Fig. 6(c)], and experiment [Fig. 6(d)]. Clearly, the CF plot does not resemble the experimental distribution of $\mathcal{E}_{CO}$, while the experimental and TSH results are qualitatively similar. For example, the maximum number of trajectories are mostly concentrated around 7–8 eV, and are mostly concentrated at a $\cos\theta$ value of -1 in both TSH and experiment.

It is interesting to understand the physical origins of the different features in the TSH plot. The low-energy but broad angular distribution arises from rotation of the CO^{2+} after both D^+ ions break off. Given the lifetime of CO^{2+}, its formation in some TSH trajectories left it with some angular momentum before dissociation. This broad distribution is not as prominent or clear in the experimental data [Fig. 6(d)].

This could be because (i) the noise in experiments hides them, (ii) the rotational timescale is comparable to the dissociation timescale of CO^{2+} (i.e., a few picoseconds), and (iii) H_2CO^{4+} may form less metastable CO^{2+} as compared to D_2CO^{4+}.

The broadness of the $\mathcal{E}_{CO}$ distribution from the TSH calculations arises from the fact that the tetracation population was formed on multiple electronic states (here six singlets and four triplets were considered in the TSH dynamics). This is clear by comparing Fig. 6(a) to Fig. 6(c), where a similar plot is plotted for the dynamics on the three lowest states, i.e., T_1, T_2, and S_0, where the $\mathcal{E}_{CO}$ distribution is much narrower. One can also notice that there are some differences in the range of $\mathcal{E}_{CO}$ distribution in the experiment and TSH calculations. There is no signal after approximately 10 eV in the latter, while in the experiment the energy extends to somewhat higher energies. This could happen because only ten states were considered for the TSH dynamics. The inclusion of more electronic states in TSH can make the $\mathcal{E}_{CO}$ distribution broader, bringing it into closer agreement with the experiment. Another reason for discrepancies between experiments and TSH results can be that all the states were equally populated with 200 initial trajectories to do the dynamics. Knowing the ionization probability to ionize CD_2O to a certain state of the tetracation can improve the TSH results. However, it is very difficult to guess the probability during strong-field ionization due to the complications that can arise during such processes [54]. Hence, the simplest way to analyze the calculations was to assume that all the states were equally populated and vertically ionized.

IV. CONCLUSION

In summary, in this work a comparison between theoretical calculations and experiment demonstrated that a simple classical description of the dynamics of Coulomb explosion using classical forces and the assumption that a single charge exists on each atom is not adequate. The presence of metastable fragments requires a quantum-mechanical description of the bonding between atoms. Furthermore, the results also indicate that ionization to multiple electronic states occurs. These results provide important insight into how to properly model Coulomb-explosion imaging, in order to properly utilize the technique to obtain structures of molecules.

ACKNOWLEDGMENTS

The authors gratefully acknowledge the US Department of Energy Office of Science for financial support through Awards No. DE-FG02-08ER15983 (V.S. and S.M.) and No. DE-FG02-08ER15984 (C.C. and T.W.). Part of the computational work was performed using the Expanse at San Diego Supercomputer Center through Grant No. CHE140114 from the Advanced Cyberinfrastructure Coordination Ecosystem: Services & Support program, which is supported by National Science Foundation through Grants No. 2138259, No. 2138286, No. 2138307, No. 2137603, and No. 2138296 [55].

APPENDIX A: VERTICAL ENERGIES BENCHMARKED WITH DIFFERENT ACTIVE SPACES OF THE CASSCF

Presented in Table III are the vertical energies of H_2CO^{4+} (or D_2CO^{4+}) calculated with different active spaces of CASSCF. It can be seen that all levels of theory provide similar energies. However, more states were averaged than the states involved in the dynamics because higher states can get involved in the dynamics at later timescales. For example, eight singlet states were averaged to calculate the electronic

TABLE III. Energies of the tetracation states for the neutral geometry of formaldehyde calculated with different active spaces of the CASSCF. All the energies at the particular level of theory are with respect to the S_0 energy for the neutral geometry.

	Singlets	S_0	S_1	S_2	S_3	S_4	S_5
Level of theory	C_{2v} symmetry	$^1B_1$	$^1A_1$	$^1A_1$	$^1A_2$	$^1A_1$	$^1B_2$
5SA-CAS(6,6)/cc-pvdz		0.00	0.22	0.59	0.93	2.51	
5SA-CAS(6,8)/cc-pvdz		0.00	0.17	0.82	0.83	2.55	
8SA-CAS(8,8)/cc-pvdz[a]		0.00	0.29	0.52	0.93	2.15	2.71
20SA-CAS(8,8)/cc-pvdz[b]		0.00	0.19	0.43	0.90	2.24	2.68
	Triplets	T_1	T_2	T_3	T_4		
Level of theory	C_{2v} symmetry	$^3B_1$	$^3A_2$	$^3B_2$	$^3B_1$		
4SA-CAS(6,6)/cc-pvdz		−1.72	−0.26	0.21	1.38		
6SA-CAS(8,8)/cc-pvdz[c]		−1.52	−0.33	0.22	1.25		
20SA-CAS(8,8)/cc-pvdz[d]		−1.60	−0.37	0.24	1.22		
	Quintets	Q_1	Q_2	Q_3	Q_4		
Level of theory	C_{2v} symmetry	$^5B_1$	$^5A_1$	$^5A_2$	$^5A_1$		
4SA-CAS(8,8)/cc-pvdz		1.53	3.69	4.01	4.48		

[a]Used for TSH dynamics.
[b]Used for PES calculations.
[c]Used for TSH dynamics.
[d]Used for PES calculations.

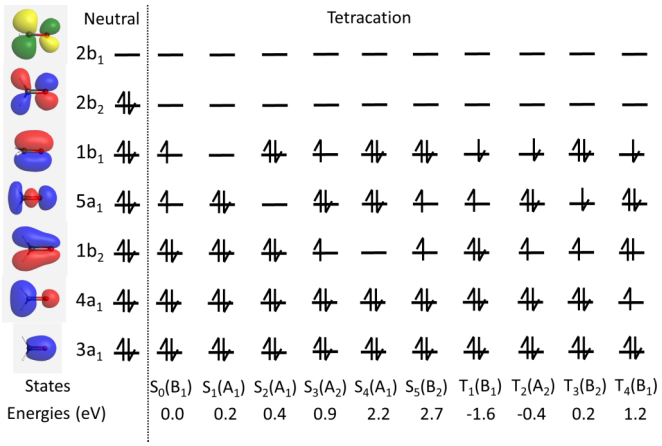

FIG. 7. Electronic configuration of first six singlets and four triplets for the neutral geometry of CH_2O^{4+}. The electronic configuration of the ground state S_0 of CH_2O is also provided, separated by a dashed line on the left-hand side.

energies of six singlets that were involved in the TSH dynamics. Similarly, six triplet states were averaged to do the TSH dynamics with four triplets. Note that the quintets are higher in energy and hence were not considered for the dynamics.

APPENDIX B: ELECTRONIC CONFIGURATIONS OF STATES OF H_2CO^{4+}

The electronic configurations of six singlets and four triplets of H_2CO^{4+} at the neutral geometry are provided in Fig. 7. The electronic configuration of H_2CO is also provided for reference. This can help readers identify the symmetry as well as the character of the states provided the holes in the orbitals. For example, the S_0 state has a hole in $5a_1$ and $1b_1$ orbitals. The tensor product of a_1 and b_1 gives the symmetry of S_0 state, which is nothing but b_1.

APPENDIX C: NATIVE FRAME ANALYSIS

The main details about the analysis have been provided in the main text. As said therein, for the theoretical analysis, the momenta of two D atoms, C, and O were taken from the last step of the TSH trajectories and then simulated with CF in order to get the final momenta of the four bodies when they are far away and there are no interactions between them. However, there is an abrupt change from a PES calculated using quantum chemistry and CF, as seen in Fig. 8. Hence, the $\mathcal{E}_{CO}$ values were shifted down with the difference between the QPES and CPES at the last point of the TSH trajectory (shown with the double-headed dashed arrow in Fig. 8). The computed data were then distributed into 2D bins of $\mathcal{E}_{CO}$ and $\cos\theta$ with bin sizes of 0.5 eV and 0.1, respectively. Also, in the case of TSH trajectories that ended with CO^{2+}, the value in each bin was distributed equally to all the $\cos\theta$ bins by dividing it by the total number of bins (which equals 20 here). The idea of equally spreading the $\cos\theta$ value among all the bins is to conserve the angular momentum of rotating CO^{2+} among all the θ values. The final distribution is normalized with respect to the maximum $\mathcal{E}_{CO}$ value and mirrored around the -1 value of $\cos\theta$.

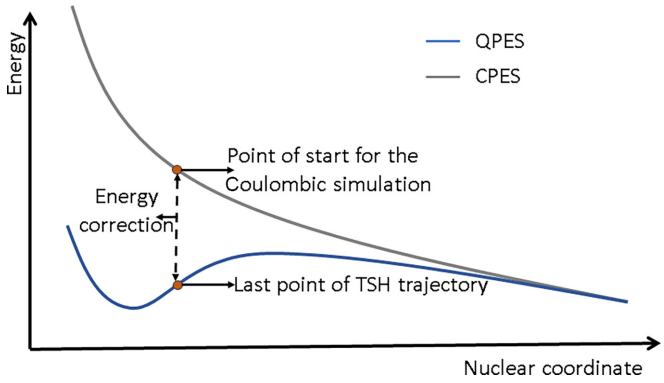

FIG. 8. Cartoon explaining the correction in energy shift made to $\mathcal{E}_{CO}$. QPES and CPES stand for quantum PES and Coulombic PES, respectively.

APPENDIX D: TSH DYNAMICS OF OTHER ELECTRONIC STATES OF D_2CO^{4+}

Figure 9 shows the evolution of the C-O bond length vs time for the dynamics run on different electronic states. It can be seen that metastable CO_2^+ is being formed on each electronic state.

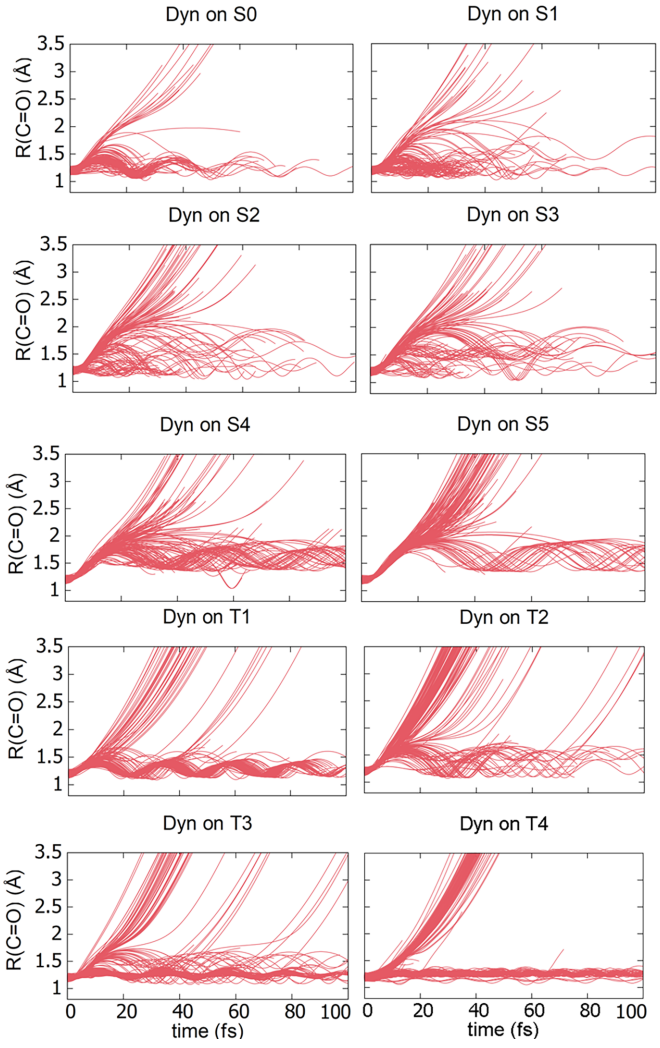

FIG. 9. Plot of C-O vs time for TSH dynamics run on different electronic states.

[1] Z. Vager, R. Naaman, and E. Kanter, Coulomb explosion imaging of small molecules, Science **244**, 426 (1989).

[2] R. Boll, J. M. Schäfer, B. Richard, K. Fehre, G. Kastirke, Z. Jurek, M. S. Schöffler, M. M. Abdullah, N. Anders, T. M. Baumann *et al.*, X-ray multiphoton-induced Coulomb explosion images complex single molecules, Nat. Phys. **18**, 423 (2022).

[3] F. Légaré, K. F. Lee, I. V. Litvinyuk, P. W. Dooley, S. S. Wesolowski, P. R. Bunker, P. Dombi, F. Krausz, A. D. Bandrauk, D. M. Villeneuve, and P. B. Corkum, Laser Coulomb-explosion imaging of small molecules, Phys. Rev. A **71**, 013415 (2005).

[4] H. Stapelfeldt, E. Constant, H. Sakai, and P. B. Corkum, Time-resolved Coulomb explosion imaging: A method to measure structure and dynamics of molecular nuclear wave packets, Phys. Rev. A **58**, 426 (1998).

[5] M. Pitzer, M. Kunitski, A. S. Johnson, T. Jahnke, H. Sann, F. Sturm, L. P. H. Schmidt, H. Schmidt-Böcking, R. Dörner, J. Stohner *et al.*, Direct determination of absolute molecular stereochemistry in gas phase by Coulomb explosion imaging, Science **341**, 1096 (2013).

[6] U. Ablikim, C. Bomme, H. Xiong, E. Savelyev, R. Obaid, B. Kaderiya, S. Augustin, K. Schnorr, I. Dumitriu, T. Osipov *et al.*, Identification of absolute geometries of *cis* and *trans* molecular isomers by Coulomb explosion imaging, Sci. Rep. **6**, 38202 (2016).

[7] S. Pathak, R. Obaid, S. Bhattacharyya, J. Buürger, X. Li, J. Tross, T. Severt, B. Davis, R. C. Bilodeau, C. A. Trallero-Herrero *et al.*, Differentiating and quantifying gas-phase conformational isomers using Coulomb explosion imaging, J. Phys. Chem. Lett. **11**, 10205 (2020).

[8] C. A. Schouder, A. S. Chatterley, J. D. Pickering, and H. Stapelfeldt, Laser-induced Coulomb explosion imaging of aligned molecules and molecular dimers, Annu. Rev. Phys. Chem. **73**, 323 (2022).

[9] A. Matsuda, M. Fushitani, E. J. Takahashi, and A. Hishikawa, Visualizing hydrogen atoms migrating in acetylene dication by time-resolved three-body and four-body Coulomb explosion imaging, Phys. Chem. Chem. Phys. **13**, 8697 (2011).

[10] R. Itakura, P. Liu, Y. Furukawa, T. Okino, K. Yamanouchi, and H. Nakano, Two-body Coulomb explosion and hydrogen migration in methanol induced by intense 7 and 21 fs laser pulses, J. Chem. Phys. **127**, 104306 (2007).

[11] A. Hishikawa, A. Matsuda, M. Fushitani, and E. J. Takahashi, Visualizing recurrently migrating hydrogen in acetylene dication by intense ultrashort laser pulses, Phys. Rev. Lett. **99**, 258302 (2007).

[12] I. Luzon, E. Livshits, K. Gope, R. Baer, and D. Strasser, Making sense of Coulomb explosion imaging, J. Phys. Chem. Lett. **10**, 1361 (2019).

[13] T. Endo, S. P. Neville, V. Wanie, S. Beaulieu, C. Qu, J. Deschamps, P. Lassonde, B. E. Schmidt, H. Fujise, M. Fushitani *et al.*, Capturing roaming molecular fragments in real time, Science **370**, 1072 (2020).

[14] M. Corrales, J. González-Vázquez, R. De Nalda, and L. Bañares, Coulomb explosion imaging for the visualization of a conical intersection, J. Phys. Chem. Lett. **10**, 138 (2019).

[15] C. S. Slater, S. Blake, M. Brouard, A. Lauer, C. Vallance, C. S. Bohun, L. Christensen, J. H. Nielsen, M. P. Johansson, and H. Stapelfeldt, Coulomb-explosion imaging using a pixel-imaging mass-spectrometry camera, Phys. Rev. A **91**, 053424 (2015).

[16] M. Burt, R. Boll, J. W. Lee, K. Amini, H. Köckert, C. Vallance, A. S. Gentleman, S. R. Mackenzie, S. Bari, C. Bomme *et al.*, Coulomb-explosion imaging of concurrent CH_2BrI photodissociation dynamics, Phys. Rev. A **96**, 043415 (2017).

[17] M. E. Corrales, G. Gitzinger, J. González-Vázquez, V. Loriot, R. de Nalda, and L. Banares, Velocity map imaging and theoretical study of the Coulomb explosion of CH_3I under intense femtosecond IR pulses, J. Phys. Chem. A **116**, 2669 (2012).

[18] W. Zhou, L. Ge, G. A. Cooper, S. W. Crane, M. H. Evans, M. N. Ashfold, and C. Vallance, Coulomb explosion imaging for gas-phase molecular structure determination: An *ab initio* trajectory simulation study, J. Chem. Phys. **153**, 184201 (2020).

[19] M. Barbatti, Nonadiabatic dynamics with trajectory surface hopping method, WIRES Comput. Mol. Sci. **1**, 620 (2011).

[20] J. C. Tully, Perspective: Nonadiabatic dynamics theory, J. Chem. Phys **137**, 22A301 (2012).

[21] C. Cheng, L. J. Frasinski, G. Moğol, F. Allum, A. J. Howard, D. Rolles, P. H. Bucksbaum, M. Brouard, R. Forbes, and T. Weinacht, Multiparticle cumulant mapping for Coulomb explosion imaging, Phys. Rev. Lett. **130**, 093001 (2023).

[22] T. Ziegler, Approximate density functional theory as a practical tool in molecular energetics and dynamics, Chem. Rev. **91**, 651 (1991).

[23] W. Kohn, A. D. Becke, and R. G. Parr, Density functional theory of electronic structure, J. Phys. Chem. **100**, 12974 (1996).

[24] A. D. Becke, Density-functional thermochemistry. III. The role of exact exchange, J. Chem. Phys. **98**, 5648 (1993).

[25] A. D. Becke, Density-functional exchange-energy approximation with correct asymptotic behavior, Phys. Rev. A **38**, 3098 (1988).

[26] C. Lee, W. Yang, and R. G. Parr, Development of the Colle-Salvetti correlation-energy formula into a functional of the electron density, Phys. Rev. B **37**, 785 (1988).

[27] S. H. Vosko, L. Wilk, and M. Nusair, Accurate spin-dependent electron liquid correlation energies for local spin density calculations: A critical analysis, Can. J. Phys. **58**, 1200 (1980).

[28] T. Clark, J. Chandrasekhar, G. W. Spitznagel, and P. V. R. Schleyer, Efficient diffuse function-augmented basis sets for anion calculations. III. The 3-21+G basis set for first-row elements, Li–F, J. Comput. Chem. **4**, 294 (1983).

[29] R. Krishnan, J. S. Binkley, R. Seeger, and J. A. Pople, Self-consistent molecular orbital methods. XX. A basis set for correlated wave functions, J. Chem. Phys. **72**, 650 (1980).

[30] B. O. Roos, P. R. Taylor, and P. E. Sigbahn, A complete active space SCF method (CASSCF) using a density matrix formulated super-CI approach, Chem. Phys. **48**, 157 (1980).

[31] T. H. Dunning, Gaussian basis sets for use in correlated molecular calculations. I. The atoms boron through neon and hydrogen, J. Chem. Phys. **90**, 1007 (1989).

[32] M. J. Frisch, G. W. Trucks, H. B. Schlegel, G. E. Scuseria, M. A. Robb, J. R. Cheeseman, G. Scalmani, G. A. P. V. Barone, H. Nakatsuji, X. Li *et al.*, *Gaussian 09, revision B.01* (Gaussian, Inc., Wallingford, 2009).

[33] H. Lischka, R. Shepard, R. M. Pitzer, I. Shavitt, M. Dallos, T. Müller, P. G. Szalay, M. Seth, G. S. Kedziora, S. Yabushita, and Z. Zhang, High-level multireference methods in the quantum-chemistry program system COLUMBUS: Analytic MR-CISD

and MR-AQCC gradients and MR-AQCC-LRT for excited states, GUGA spin-orbit CI and parallel CI density, Phys. Chem. Chem. Phys. **3**, 664 (2001).

[34] H. Lischka, R. Shepard, I. Shavitt, R. M. Pitzer, M. Dallos, T. Müller, P. G. Szalay, F. B. Brown, R. Ahlrichs, H. J. Böhm *et al.*, COLUMBUS, an *ab initio* electronic structure program, release 7.0 (2017).

[35] H. Lischka, R. Shepard, T. Müller, P. Szalay, R. Pitzer, A. Aquino, M. do Nascimento, M. Barbatti, L. Belcher, J. Blaudeau *et al.*, The generality of the GUGA MRCI approach in COLUMBUS for treating complex quantum chemistry, J. Chem. Phys. **152**, 134110 (2020).

[36] M. Barbatti, M. Ruckenbauer, F. Plasser, J. Pittner, G. Granucci, M. Persico, and H. Lischka, Newton-X: A surface-hopping program for nonadiabatic molecular dynamics, WIRES Comput. Mol. Sci. **4**, 26 (2014).

[37] M. Barbatti, M. Bondanza, R. Crespo-Otero, B. Demoulin, P. O. Dral, G. Granucci, F. Kossoski, H. Lischka, B. Mennucci, S. Mukherjee *et al.*, Newton-X platform: New software developments for surface hopping and nuclear ensembles, J. Chem. Theory Comput. **18**, 6851 (2022).

[38] J. C. Tully, Molecular dynamics with electronic transitions, J. Chem. Phys. **93**, 1061 (1990).

[39] G. Granucci and M. Persico, Critical appraisal of the fewest switches algorithm for surface hopping, J. Chem. Phys. **126**, 134114 (2007).

[40] C. Zhu, S. Nangia, A. W. Jasper, and D. G. Truhlar, Coherent switching with decay of mixing: An improved treatment of electronic coherence for non-Born–Oppenheimer trajectories, J. Chem. Phys. **121**, 7658 (2004).

[41] A. T. Eppink and D. H. Parker, Velocity map imaging of ions and electrons using electrostatic lenses: Application in photoelectron and photofragment ion imaging of molecular oxygen, Rev. Sci. Instrum. **68**, 3477 (1997).

[42] A. Zhao, M. van Beuzekom, B. Bouwens, D. Byelov, I. Chakaberia, C. Cheng, E. Maddox, A. Nomerotski, P. Svihra, J. Visser *et al.*, Coincidence velocity map imaging using Tpx3Cam, a time stamping optical camera with 1.5 ns timing resolution, Rev. Sci. Instrum. **88**, 113104 (2017).

[43] A. Catanese, B. Kaufman, C. Cheng, E. Jones, M. G. Cohen, and T. Weinacht, Acousto-optic modulator pulse-shaper compression of octave-spanning pulses from a stretched hollow-core fiber, OSA Continuum **4**, 3176 (2021).

[44] M. Nisoli, S. De Silvestri, and O. Svelto, Generation of high energy 10 fs pulses by a new pulse compression technique, Appl. Phys. Lett. **68**, 2793 (1996).

[45] T. Nagy, P. Simon, and L. Veisz, High-energy few-cycle pulses: Post-compression techniques, Adv. Phys.-X **6**, 1845795 (2021).

[46] T. Nagy, M. Forster, and P. Simon, Flexible hollow fiber for pulse compressors, Appl. Opt. **47**, 3264 (2008).

[47] C. Cheng, R. Forbes, A. J. Howard, M. Spanner, P. H. Bucksbaum, and T. Weinacht, Momentum-resolved above-threshold ionization of deuterated water, Phys. Rev. A **102**, 052813 (2020).

[48] F. Penent, R. I. Hall, R. Panajotović, J. H. D. Eland, G. Chaplier, and P. Lablanquie, New method for the study of dissociation dynamics of state-selected doubly charged ions: Application to CO^{2+}, Phys. Rev. Lett. **81**, 3619 (1998).

[49] M. Lundqvist, P. Baltzer, D. Edvardsson, L. Karlsson, and B. Wannberg, Novel time of flight instrument for Doppler free kinetic energy release spectroscopy, Phys. Rev. Lett. **75**, 1058 (1995).

[50] L. H. Andersen, J. H. Posthumus, O. Vahtras, H. Ågren, N. Elander, A. Nunez, A. Scrinzi, M. Natiello, and M. Larsson, Very slow spontaneous dissociation of CO^{2+} observed by means of a heavy ion storage ring, Phys. Rev. Lett. **71**, 1812 (1993).

[51] J. P. Bouhnik, I. Gertner, B. Rosner, Z. Amitay, O. Heber, D. Zajfman, E. Y. Sidky, and I. Ben-Itzhak, Measurements of the mean lifetime and kinetic-energy release of metastable CO^{2+}, Phys. Rev. A **63**, 032509 (2001).

[52] T. Šedivcová, P. Žďánská, V. Špirko, and J. Fišer, Computed lifetimes of metastable states of CO^{2+}, J. Chem. Phys. **124**, 214303 (2006).

[53] J. Rajput, T. Severt, B. Berry, B. Jochim, P. Feizollah, B. Kaderiya, M. Zohrabi, U. Ablikim, F. Ziaee, K. R. P. *et al.*, Native frames: Disentangling sequential from concerted three-body fragmentation, Phys. Rev. Lett. **120**, 103001 (2018).

[54] C. Cheng, Z. L. Streeter, A. J. Howard, M. Spanner, R. R. Lucchese, C. W. McCurdy, T. Weinacht, P. H. Bucksbaum, and R. Forbes, Strong-field ionization of water. II. Electronic and nuclear dynamics en route to double ionization, Phys. Rev. A **104**, 023108 (2021).

[55] T. J. Boerner, S. Deems, T. R. Furlani, S. L. Knuth, and J. Towns, *PEARC 2023—Computing for the Common Good: Practice and Experience in Advanced Research Computing, Portland, 2023* (ACM, New York, 2023), pp. 173–176.